RESEARCH ARTICLE

Self-Powered Airflow Sensor Based on Energy Harvesting of Ventilation Air in Buildings

Moon Hyun Chung[1,2] · Seunghwan Yoo[2] · Woo-Nam Jung[3,4] · Hakgeun Jeong[2] · Kyung-Hwa Yoo[1]

Abstract

Heating, ventilation, and air conditioning (HVAC) systems account for one-third of the total energy consumption in office buildings. The use of airflow measurements to control the operation of HVAC systems can reduce energy consumption; thus, a sensor capable of monitoring airflow in a duct system is critical. Triboelectric nanogenerators (TENGs) can be utilized as self-powered sensors in airflow-driven TENGs (ATENGs) as self-powered sensors. By employing ferroelectric materials and surface modifications, the surface charges of TENGs can be increased. In this study, fibrous-mat TENGs were prepared using ferroelectric materials consisting of poly (vinylidene fluoride-co-trifluoroethylene) (PVDF-TrFE) and polyamide 11 (nylon-11). And these materials were subsequently investigated. Poly (3,4-ethylenedioxythiophene):poly(styrenesulfonate) was added to PVDF-TrFE to enhance the ferroelectric crystalline phase. X-ray diffraction analysis revealed that this incorporation affects the β phase. In addition, the surface of nylon-11 was modified using the electrospray technique for post-treatment, thereby improving the interfacial adhesion between the fibers. These materials were then utilized in fibrous-mat ATENGs (FM-ATENGs) to demonstrate their practical application. The FM-ATENGs can be effectively used in an Arduino airflow-check sensor, showcasing their potential for application in HVAC systems, to enhance airflow control and energy efficiency.

Keywords HVAC · Airflow-driven triboelectric nanogenerator · Building energy harvesting · Fibrous mat · Airflow sensor

Introduction

Heating, ventilation, and air conditioning (HVAC) systems account for approximately 40% of the energy consumption in commercial buildings [1, 2]. Airflows generated by HVAC systems are widely used to maintain comfortable indoor environments in terms of temperature, humidity, and air quality in buildings [3, 4]. In a typical office building, the airflow generated at the end of the duct is between 2 and 4 m/s [5]. Therefore, monitoring the volumetric airflow by calculating the airflow velocity and duct size can enhance energy savings in office buildings through improved HVAC maintenance and efficiency. Maintaining a primary battery in an airflow-check sensor poses challenges, making energy harvesting technologies crucial. These technologies help reduce the frequency of primary battery replacement or enable the charging of secondary batteries in sensor devices [6]. Thus, an airflow-based energy harvesting technology is required.

Triboelectric nanogenerators (TENGs) [7–9] are energy harvesting devices that can be used in self-powered devices [10–12] or sensors [13–15]. TENGs convert mechanical energy into electrical energy [16, 17]. In the case of sensors, TENGs can detect pressure states based on the triboelectric voltage output [18]. Additionally, using the conducting properties of triboelectric materials, the electrical output can be used to detect the presence of bacteria [19].

✉ Hakgeun Jeong
   hgjeong@kier.re.kr

✉ Kyung-Hwa Yoo
   khyoo@yonsei.ac.kr

1 Department of Physics, Yonsei University, 50 Yonsei-Ro, Seodaemun-Gu, Seoul 03722, Republic of Korea

2 Energy ICT Convergence Research Department, Energy Efficiency Research Division, Korea Institute of Energy Research, 152 Gajeong-Ro, Yuseong-Gu, Daejeon 34129, Republic of Korea

3 Advanced Combustion Power Lab, Energy Efficiency Research Division, Korea Institute of Energy Research, 152, Gajeong-Ro, Yuseong-Gu, Daejeon 34129, Republic of Korea

4 Department of Mechanical Engineering, Korea Advanced Institute of Science and Technology (KAIST), 291 Daehak-Ro, Yuseong, Daejeon 34141, Republic of Korea

For airflow-driven TENGs (ATENGs), energy is harvested through flutter and rotation [20]. Among the sliding working modes, the rotational type ATENG efficiently generates energy. The energy generated by a flutter-type ATENG is lower than that generated by the rotational type; nevertheless, the flutter-type ATENG has advantages such as smaller size requirements and stackability [21].

TENGs rely on triboelectrification and electrostatic induction [22]. The electrical output performance of TENGs is affected by surface charges [23], which can be enhanced through the use of composite materials, structures, and surface modifications [24, 25]. One technique for surface structure modification [26] involves obtaining fibrous mats through electrospinning. These mats are inexpensive, easy to fabricate, and possesses high surface roughness values and large surface areas [27]. Moreover, larger contact surface areas can improve the electrical output performance of TENGs [28]. However, fibrous mats exhibit weak interfacial adhesion between substrates and low mechanical strength when in contact with TENGs, leading to reduced reliability and performance [29, 30]. Therefore, post-processing operations, such as hot pressing, annealing, solvent welding, and chemical crosslinking, are required to enhance the surface properties of fibrous mats [31, 32]. In addition, the stability of fibrous mats can be increased by incorporating self-healing properties [33].

Furthermore, the introduction of ferroelectric materials can increase the surface potential and residual dielectric polarization through the dipole coupling effect [34, 35]. The ferroelectric polymers studied include polyvinylidene fluoride (PVDF), polyamide (nylon), polylactic acid, and polylactic glycolic acid [36]. PVDF can be utilized to modify molecular structure, create composites, or enhance ferroelectric properties by incorporating nanofillers [37]. Nylon is a tribopositive material in the triboelectric series and contains carbon atoms with repeated even and odd numbers. The dipole moments of amide groups depend on the number of carbon atoms; therefore, as opposed to even-numbered nylon, odd-numbered nylon enhances ferroelectric properties [38, 39].

In this study, poly (vinylidene fluoride-co-trifluoroethylene) (PVDF-TrFE) and odd-numbered nylon (nylon-11) were used to create a fibrous mat via electrospinning and electrospraying. In addition, poly (3,4-ethylenedioxythiophene):poly(styrenesulfonate) (PEDOT:PSS) nanofillers were added to the PVDF-TrFE composite solution to improve its ferroelectric properties, based on our previous research [40]. The surface of the target material was modified through post-treatment electrospraying of the nylon-11 fibrous mat. Next, the effect of the PVDF-TrFE/PEDOT:PSS composite and nylon-11 fibrous mat on the ferroelectric crystallization of phase was examined using Fourier-transform infrared spectroscopy (FT-IR) and X-ray diffraction (XRD). In

addition, the surface potential of the fibrous mats was measured via atomic force microscopy, specifically Kelvin probe force microscopy (KPFM), to confirm their position in the triboelectric series. The electrospraying and electrospinning times for the nylon-11 and PVDF-TrFE/PEDOT:PSS fibrous mats were respectively optimized. The electrical output performances of the nylon-11 and PVDF-TrFE/PEDOT:PSS fibrous mats were measured in the contact–separation mode of the TENG. Furthermore, fibrous mat ATENGs (FM-ATENGs) were fabricated using the aforementioned fibrous mats. The optimal height of the FM-ATENGs was determined through simulations, and the electrical output performance was measured at airflow velocities ranging from 2 to 5 m/s. The airflow-check sensors were powered by the energy generated by the FM-ATENGs. An Arduino was incorporated to act as a switch for the airflow-check sensors and used to transmit the airflow data to a mobile phone.

Experimental Section

Materials

PEDOT:PSS (Clevios PH1000) and PVDF-TrFE (70–30 mol.%) copolymer powders were purchased from Heraeus (Germany) and Piezotech (France), respectively. Nylon-11, acetone, dimethylformamide (DMF), dichloromethane, formic acid, and a polyethylene terephthalate (PET)/indium tin oxide (ITO) film (125 μm, 60 Ω/sq) were obtained from Sigma–Aldrich. Silicone rubber sheets (Si rubber, 100 μm) were obtained from AlphaFlon (Republic of Korea). Conductive Cu foil tape (Cu tape, 80 μm) was purchased from 3 M (USA).

Fabrication of PVDF-TrFE/PEDOT:PSS Fibrous Mat

PVDF-TrFE/PEDOT:PSS electrospinning solutions were prepared in the same manner as in our previous study [40]. In brief, PEDOT:PSS solution (0.4 g) in water was dispersed in DMF and acetone (10 mL; 2:3 volume ratio), and PVDF-TrFE copolymer powder (2 g) was added to the PEDOT:PSS/DMF/acetone solution, which was then stirred for 12 h at 35 ℃. A 20-gauge blunt needle was used to load the prepared solution into a syringe. Electrospinning was performed on Al foil at a voltage of 7 kV, flow rate of 0.3 mL/h, and needle-to-plate distance of 15 cm. It was then evaporated for 2 h in a vacuum chamber and annealed for 1 h at 90 °C on a hotplate (Fig. S1).

Fabrication of Nylon-11 Fibrous Mat

To prepare the nylon-11 electrospinning solution (12 wt.%), nylon-11 pellets were dissolved in dichloromethane and

formic acid (2:1 volume ratio) at 25 ℃. To prepare the nylon-11 electrospray solution (12 wt.%), formic acid was mixed with nylon-11 pellets and the solution was stirred for 2 h at 70 °C. The electrospinning and electrospray solutions were injected into a syringe using a 20-gauge blunt needle. Electrospinning was performed on ITO/PET at a supplied voltage of 6.5 kV, flow rate of 0.3 mL/h, and needle-to-plate distance of 10 cm. Subsequently, electrospraying was performed on the nylon-11 electrospun mat/ITO/PET at a supplied voltage of 15 kV, flow rate of 1 mL/h, and needle-to-plate distance of 10 cm (Fig. S2). The nylon-11 fibrous mat was then dried in a vacuum oven for 2 h at 50 ℃.

Fabrication of FM-TENG

The fibrous mat TENG (FM-TENG) was fabricated in the contact–separation mode using PVDF-TrFE/PEDOT:PSS fibrous mat/Si rubber/Cu tape/PET (30×30 mm^2) and nylon-11 fibrous mat/ITO/PET (50×50 mm^2), resulting in an effective contact area of 30×30 mm^2.

Fabrication of FM-ATENG

The FM-ATENG consisted of a PVDF-TrFE/PEDOT:PSS fibrous mat on Si rubber, a nylon-11 fibrous mat, an ITO/PET electrode, and a polycarbonate (PC) shell. A PC cuboid with dimensions of $45 \times 100 \times 46$ mm^3 (inner dimensions of $30 \times 100 \times 30$ mm^3; width (W) $\times$ length (L) $\times$ height (H), respectively) was formed. Cu tape was used to adhere the PVDF-TrFE/PEDOT:PSS/Si rubber (30×100 mm^2) to the middle plane of the PC cuboid. Next, a piece of nylon-11 fibrous mat/ITO/PET (30×100 mm^2) was attached to the top and bottom of the PC plates. The PVDF-TrFE/PEDOT:PSS fibrous mat on Si rubber was used for flutter. Cu wires were used to connect the electrodes.

Characterization

Field-emission scanning electron microscopy (FE-SEM; JSM-6500F, JEOL, Japan) was used to analyze the surface morphology. The surface potential characteristics of the PVDF-TrFE/PEDOT:PSS and nylon-11 films were measured using KPFM (NX-10, Park Systems, Republic of Korea), XRD (D/max-2500 pc, Rigaku, Japan), and FT–IR spectroscopy (Nicolet iS50, Thermo Fisher Scientific Instruments, USA) to investigate the structures of the composite films. An oscilloscope (DPO 2002 B, 40 MΩ probe, Tektronix, USA), a low-noise current preamplifier (Model SR 570, Stanford Research Systems, Inc., USA), and an electrometer (6514, Keithley, USA) were used to measure the output performance of the TENGs. A function generator and mechanical wave driver (PI-8127 and SF-9324, PASCO, USA) were

used to provide motion to the FM-TENG. Airflow velocity was estimated using a vane anemometer (AVM-03, PROVA, Taiwan).

Results and Discussion

Figure 1a shows a schematic of the FM-ATENG structure. The insets show FE-SEM images of the nylon-11 and PVDF-TrFE/PEDOT:PSS fibrous mats. The PVDF-TrFE/PEDOT:PSS fibrous mat consists of uniform fibers with an average diameter of 500 nm (Fig. S1). Electrospinning and electrospraying were employed to produce a nylon-11 fibrous mat on the ITO/PET films. Furthermore, post-treatment was performed using the electrospray method at time intervals ranging from 10 s to 5 min (Fig. S2). This resulted in the formation of nylon-11 particles on the nylon-11 fibrous mat, (Fig. S3a–e) which presented as welding (red arrows in Fig. S3f).

The FM-ATNEGs are in the shape of the PC cuboid and images of the fabricated FM-ATENG are shown in Fig. 1b. For this configuration, the wind-speed effect depended on the height of the internal PC cuboid. Moreover, the PC cuboid's thickness and the part of fixed flutter become a resistance to airflows. Simulation was conducted to find the airflow velocity similar to the outside and inside the PC cuboid to make the most of airflows. This was simulated using COMSOL Multiphysics with an airflow rate of 2 m/s and the height of the PC cuboid ranging from approximately 1 to 5 cm (Fig. S4). The simulation results indicate that when the internal height of the PC cuboid is less than 3 cm, the wind speed inside the PC cuboid is lower than that in the chamber. However, when the internal height of the PC cuboid is higher than 3 cm, the wind speed inside the PC cuboid is similar to that in the chamber. Consequently, the minimum height (H) of the internal PC cuboid was fixed at 3 cm, and the width (W) and length (L) were set to 3 and 10 cm, respectively.

The XRD spectra of the fibrous mat were analyzed in the 2θ range of 15–25° to investigate the ferroelectric crystalline phase (Fig. 1c). The PVDF-TrFE fibrous mat exhibits a peak at 19.8°, which can be attributed to the β phase at the (110) and (200) planes [41, 42]. The PVDF-TrFE/PEDOT:PSS fibrous mat exhibits an identical peak; however, the crystallinity of PVDF-TrFE is unaffected by the addition of PEDOT:PSS. Thus, the FT-IR and XRD analyses agree with previous findings involving PVDF-TrFE/PEDOT:PSS composite films [40]. Note that the ferroelectric property is exhibited by the pseudohexagonal δ' phase of nylon-11. Thus, the nylon-11 fibrous mat exhibits a peak at 21.6°, which corresponds to the δ' phase (Fig. 1c) at the (001) and (hk0) planes [41].
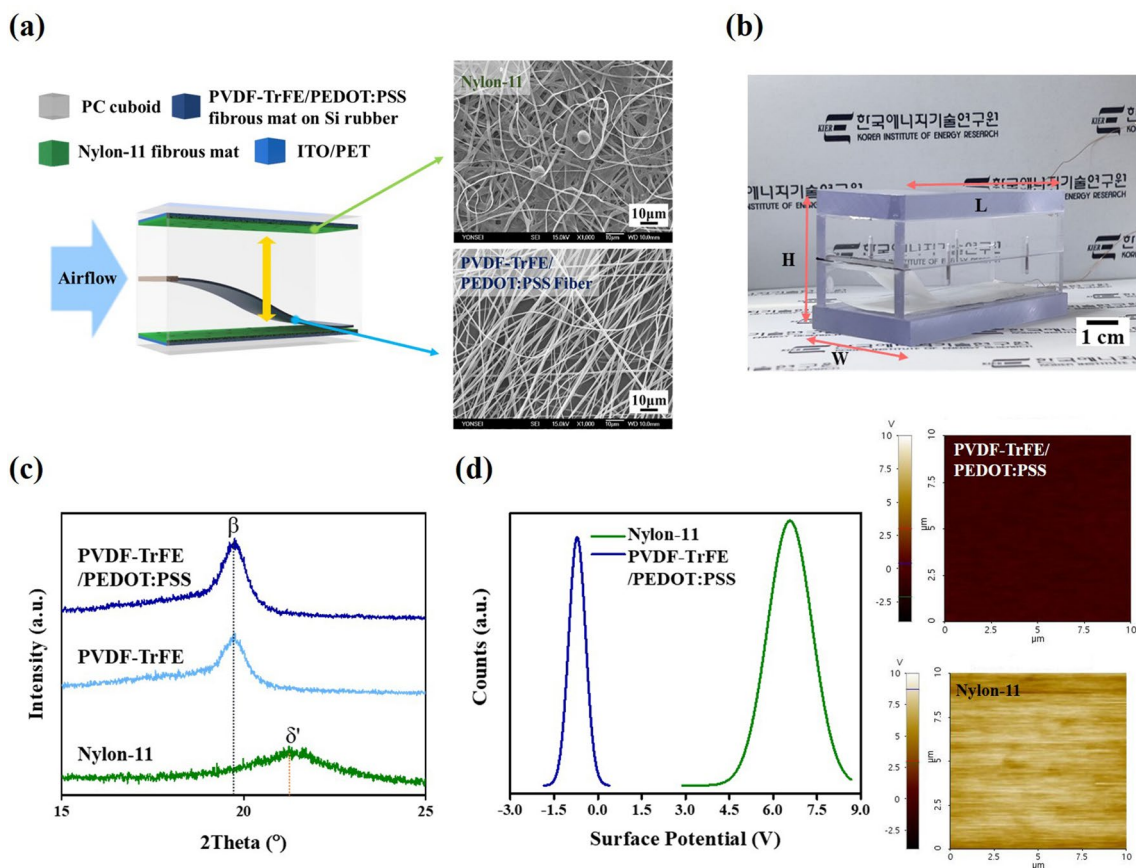
Fig. 1 **a** Schematic of the FM-ATENG. The inset shows FE-SEM images of the fibrous mats. **b** Photograph of the FM-ATENG setup. **c** XRD analysis of PVDF-TrFE/PEDOT:PSS and nylon-11 fibrous mats. **d** KPFM analysis of PVDF-TrFE/PEDOT:PSS and nylon-11

Furthermore, the PVDF-TrFE and PVDF-TrFE/PEDOT:PSS fibrous mats were analyzed using FT-IR spectra, with wavenumbers ranging from 400 to 1600 cm^{-1}, as shown in Fig. S5a. A crystalline phase is detected in the PVDF-TrFE fibrous mat, with an electroactive crystalline β phase observed in the absorption band at 840 cm^{-1}, which is characteristic of CF$_2$ symmetric stretching. In addition, peaks at 510, 1288, and 1430 cm^{-1}, which can be attributed to the β phase, and that at 763 cm^{-1}, which can be ascribed to the α phase, are observed [42, 43]. These findings were replicated in the PVDF-TrFE/PEDOT:PSS fibrous mats. The electroactive phase (β phase) fraction (F_{EA}) in the samples was estimated using the Lambert–Beer law, as shown in Eq. (1) [44]:

$$F_{EA}(\%) = \frac{I_{EA}}{\left(\frac{K_{EA}}{K_\alpha}\right)I_\alpha + I_{EA}} \times 100 \tag{1}$$

where I_α and I_{EA} denote the absorption intensities of the FT-IR peaks at 763 (α phase) and 840 cm^{-1} (β phase), respectively; and K_α and K_{EA} denote the absorption coefficients at 763 and 840 cm^{-1}; respectively, with $K_\alpha = 6.1 \times 10^4$

cm$^2 \cdot$mol^{-1} and $K_{EA} = 7.7 \times 10^4$ cm$^2 \cdot$mol^{-1} [43, 45]. The F_{EA} value decreases from 76.13% to 70.07% when PEDOT:PSS is used. Compared with that of PVDF-TrFE alone, the absorbance of the α phase at 763 cm^{-1} increases owing to the C–S–C peak of the PEDOT:PSS at 761 cm^{-1} (Fig. S5b). Fig. S5c depicts the FT-IR spectrum of the nylon-11 fibrous mat at wavenumbers ranging from 1200 to 3600 cm^{-1}. The hydrogen bonding or free amide group comprising amide I and II are responsible for the absorption band ranging from 1500 to 1700 cm^{-1}, whereas the other band is observed at 3300 cm^{-1} (amide A). The peak at 1635 cm^{-1} represents the C=O stretching modes, whereas the peak at 3300 cm^{-1} represents the N–H stretching modes. These findings support the existence of polarization in the nylon-11 fibrous mat [46].

The triboelectric series can be organized in terms of the positive and negative charges based on the surface potential of the materials. Previous research [38, 47, 48] reported that PVDF-TrFE and nylon-11 have negative and positive triboelectric charges, respectively. The surface potentials of PVDF-TrFE/PEDOT:PSS and nylon-11 were investigated using KPFM over an area of 10×10 μm^2, as shown in Fig. 1d and Fig. S5d. The surface potentials of

the PVDF-TrFE and PVDF-TrFE/PEDOT:PSS are − 2.23 and − 0.71 V, respectively, whereas nylon-11 has a positive surface potential (6.56 V). Moreover, the surface potential of the fibrous mat incorporating PEDOT:PSS shifts to a more positive position compared with that of PVDF-TrFE. Thus, the charge storage ability is increased by the PEDOT:PSS [49]. These findings confirm previously reported triboelectric series trends [22, 38, 47].
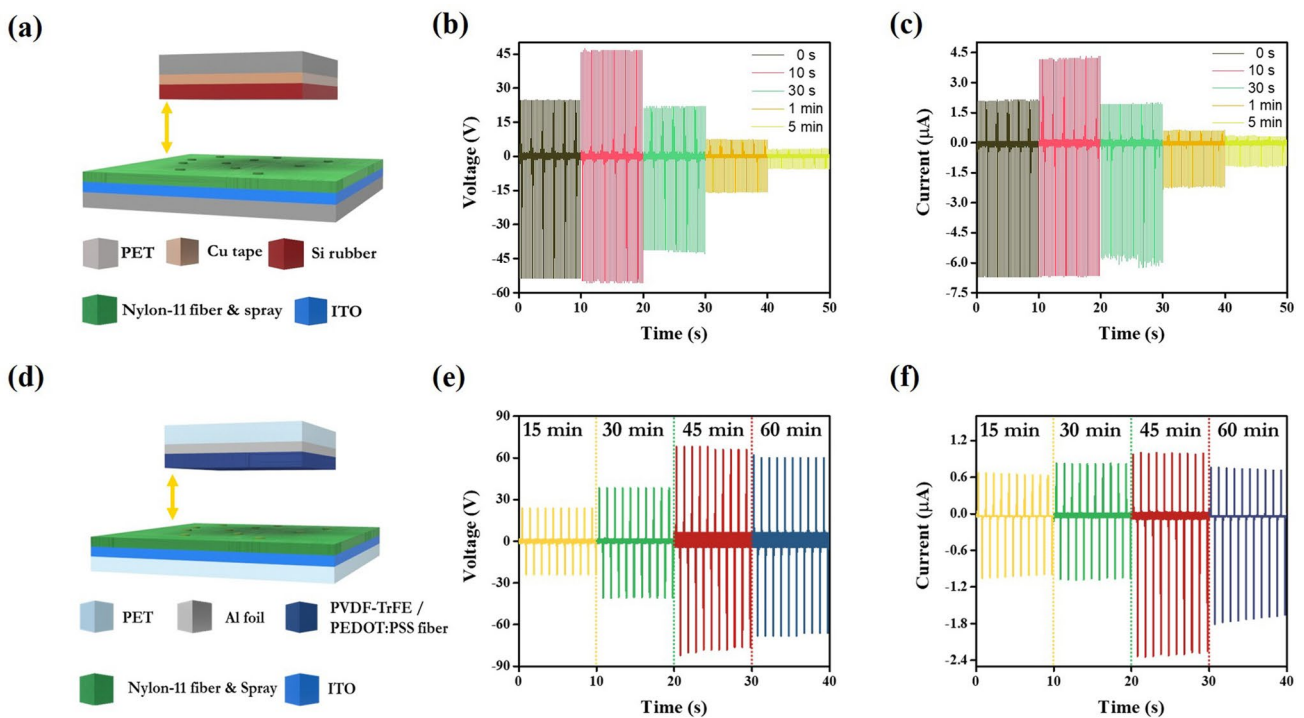
To determine the electrical output performance based on the electrospinning time of nylon-11, Si rubber was used as the friction layer with the nylon-11 fibrous mat in the contact–separation mode (Fig. S6). The applied tapping force was approximately 8 N with an oscillation frequency of 5 Hz, and the maximum contact–separation distance was set to 7 mm. The electrical output performance was evaluated by varying the electrospinning time from 1 min to 1 h. When the electrospinning time is increased to 30 min, the open-circuit voltage (V_o) and short-circuit current (I_{sc}) increase to 24 V and 2.16 µA, respectively, owing to an increase in specific area. The electrical output performances decrease to 19.2 V and 1.76 µA after 1 h of electrospinning, as shown in Fig. S6a and b.

After setting the electrospinning time to 30 min, electrospraying was performed for 10 s, with V_o and I_{sc} increasing to 46 V and 4.24 µA, respectively (Fig. 2a–c). This suggests that the electrospray method alters the nylon-11 fibrous mat and renders it a more effective contact surface. However, the electrical output performance deteriorates when electrospraying is conducted for 5 min. The electrospray solution likely reduces the effective surface area by covering the surface of the nylon-11 fibrous mat.

Figure 2d shows the schematic of the PVDF-TrFE/PEDOT:PSS fibrous mat and nylon-11 fibrous mat (electrosprayed for 10 s) TENGs. Figure 2e and f presents the V_o and I_{sc} of nylon-11 fibrous mat and PVDF-TrFE/PEDOT:PSS fibrous mats for various electrospinning durations of PVDF-TrFE/PEDOT:PSS on Al foil. The generated V_o and I_{sc} after 45 min of electrospinning of the PVDF-TrFE/PEDOT:PSS are 68 V and 0.98 µA, respectively, and after 1 h, the electrical outputs are 60 V and 0.72 µA, respectively. The thickness of the fibrous mat increases with increasing electrospinning duration; consequently, the resistance to charge transfer increases. Therefore, the ability for current to pass through thicker fibrous mats can be low that through thinner fibrous mats fabricated with optimized electrospinning times [50]. Further research is required to clarify the implications of these results in terms of the duration of electrospinning.

Furthermore, the electrical output performance of the FM-TENGs was tested to determine the effect of frequency variations, ranging from 1 to 25 Hz (Fig. S7a-c).


Fig. 2 **a** Schematic of the nylon-11 fibrous mat and Si rubber TENG. Generated electrical output performance of the Si rubber and nylon-11 fibrous mat with electrospray time: **b** open-circuit voltage and **c** short-circuit current. **d** Schematic of the PVDF-TrFE/PEDOT:PSS fibrous mat and nylon-11 fibrous mat TENG. Generated electrical output performances of TENGs with the used for PVDF-TrFE/PEDOT:PSS: **e** open-circuit voltage and **f** short-circuit current. Nylon-11 was electrosrpayed for 10 s

The electrical output performance increases significantly at higher frequencies, and the generated V_o and I_{sc} at 20 Hz are 550 V and 28 µA, respectively. This suggests that the FM-TENGs quickly reach equilibrium and increase the charge transfer rate. When the frequency is too high (> 25 Hz), the electrical output performance decreases, as it cannot recover to its original position before the next contact [51, 52]. The external load resistance (R_L) voltage was then measured from 100 kΩ to 960 MΩ, as shown in Fig. S8a. Using $P = (I^2R/$effective contact area), the estimated power density of the FM-TENG is 873 µW/cm^2 at $R_L = 5$ MΩ (Fig. S8a). The FM-TENGs were further tested for stability at 20 Hz for 2000s, demonstrating that the generated voltage was stable (Fig. S8b). Additionally, the FM-TENG capacitor charging was tested. The 470 µF capacitors charge up to 3.3 V in 400 s at 20 Hz (Fig. S8c).

Based on the experimental results, we selected the PVDF-TrFE/PEDOT:PSS fibrous mat (electrospinning time of 30 min) on Si rubber as the flutter material for the FM-ATENG, and the nylon-11 fibrous mat (electrospray time of 10 s) was used as the opposing friction material. Figure 3a shows the working mechanism of the FM-ATENG, which includes triboelectrification and electrostatic induction [53]. According to the KPFM analysis, the surface charges of PVDF-TrFE/PEDOT:PSS and nylon-11 exhibit negative and positive properties, thus

exhibiting charge generation in the following way: (i) When the PVDF-TrFE/PEDOT:PSS flutter and bottom-Nylon-11 fibrous mats are in contact, the charges remain neutral on the contact surface. (ii) When the PVDF-TrFE/PEDOT:PSS flutter is moved by the airflow to the upper-Nylon-11 fibrous mat, the generated potential difference drives the electrons from the top to the bottom of the ITO electrode via electrostatic induction. To achieve electrostatic equilibrium, electrons flow continuously to the point of maximum electrical potential. (iii) The induced charges become neutral again when the two fibrous mats come into contact. (iv) When the PVDF-TrFE/PEDOT:PSS flutter moves down to the bottom-Nylon-11 fibrous mat, the electrostatic equilibrium is disrupted, and electrons flow back from the bottom to the top of the ITO electrode. Owing to the contact–separation modes between the two different fibrous mats, this process is repeated to generate an alternating electrical output. The inset graph of Fig. 3a shows the electrical output state corresponding to each condition. The electrical output performance of the FM-ATENG was evaluated by varying the airflow from 2 to 5 m/s (Fig. S9). The flutter begins to move from 2 m/s steadily and an electrical output signal is received (Fig. 3b and Video S1). Figure 3c–f show V_o with different airflow velocities; the voltage increases from 3 to 8.8 V as airflow velocity increases from 2 to 5 m/s, indicating that the contact
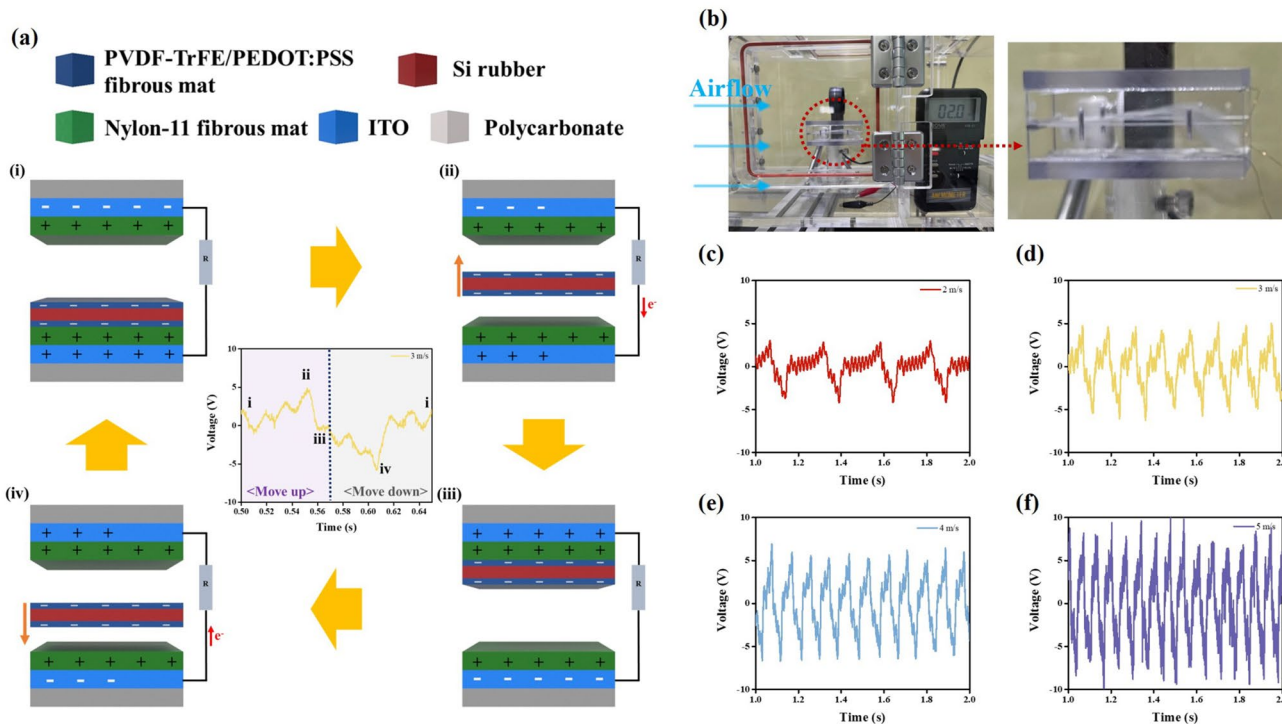
Fig. 3 a Working mechanism of the FM-ATENG prepared with the nylon-11 and PVDF-TrFE/PEDOT:PSS fibrous mats. The inset displays the electrical output state corresponding to each condition. **b** Photographs of the flutter moving under an airflow rate of 2 m/s. Open circuit voltage of the FM-ATENGs with different airflow velocities: **c** 2, **d** 3, **e** 4, and **f** 5 m/s

frequencies between the flutter and nylon-11 fibrous mat increase with increasing airflow.

Moreover, the kinetic energy of flutter increases the surface charge density as the airflow rate increases [21]. To compare the kinetic energy ($E_{kinetic}$) at the various airflow rates, Eq. (2) was used.

$$E_{kinetic} = \frac{m_f v_f^2}{2} \tag{2}$$

Here m_f is the mass of the flutter film (0.0002 kg), and V_f is the velocity of the flutter of the FM-ATENG. The velocity of flutter was obtained using $V_f = D\omega$ (D: height of flutter moving and ω: angular frequency). To simplify the calculation, the flutter was assumed to move at a constant velocity. As a result, $E_{kinetic}$ increased with an increasing

airflow rate, as presented in Table 1. In addition, the conversion efficiency was calculated using $E_{kinetic}$ and the electrical energy ($E_{electric}$) generated by the FM-ATENGs using Eq. (3):
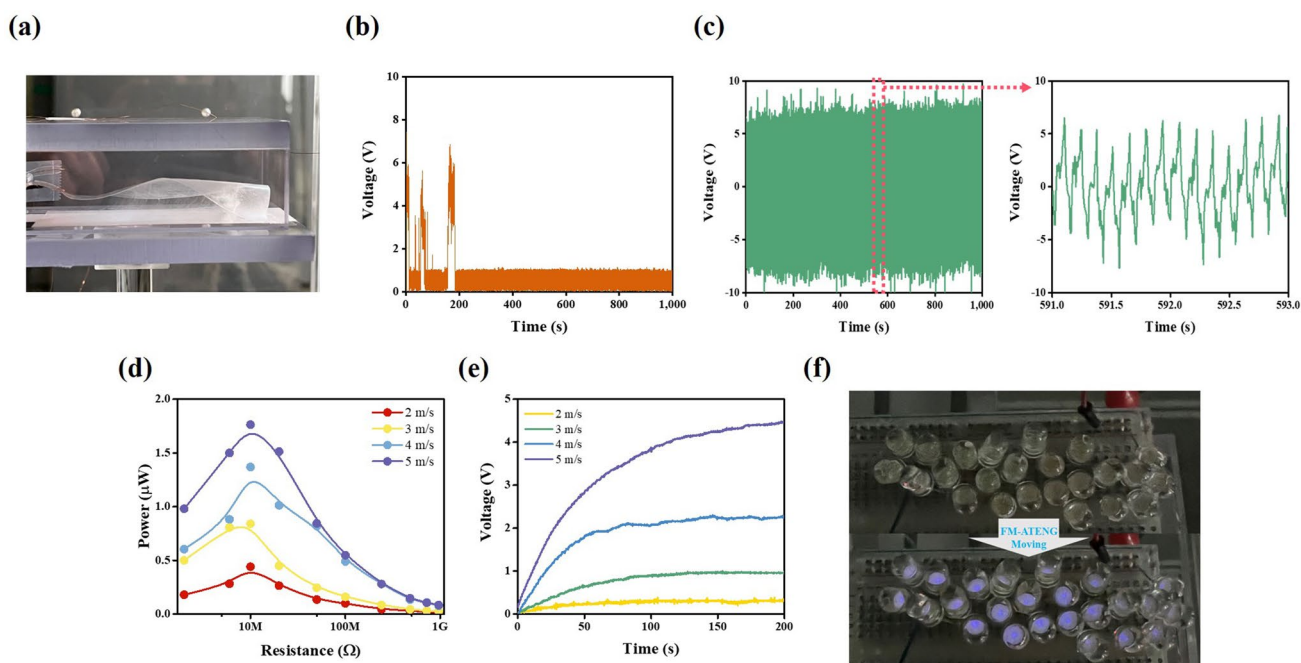
$$\eta\ (\%)\ =\ \frac{E_{electric}}{E_{kinetic}} \times 100 \tag{3}$$

The conversion efficiency increases up to a velocity of 4 m/s; however, the efficiency decreases at 5 m/s. Notably, interference in the flutter movement occurs in this FM-ATENG because of the change in Reynolds number with an increase in the airflow rate. Consequently, the amount of electrical energy is assumed to not increase significantly compared with the kinetic energy of the flutter at higher airflow velocities, thus decreasing conversion efficiency.

FM-ATENGs were preferentially prepared using non-post-treated nylon-11 fibrous mats to observe the surface modifications caused by the post-treatment. After fluttering, the fibers become electrostatically attached to the flutter and peel off from the substrates, as shown in Fig. 4a. Consequently, the flutter moves with a high resistance at a low airflow, whereas the post-treated nylon-11 fibrous mat moves easily. The post-treatment of the nylon-11 fibrous mat significantly improves the flutter stability of the FM-ATENGs compared with that of the nontreated nylon-11 fibrous mat.

Table 1 Calculated kinetic energy of the flutter and conversion efficiency of the FM-ATENG with varied airflow rates

Airflow velocity (m/s)	Velocity of flutter (m/s)	Kinetic energy (μJ)	Generated energy (μJ)	Conversion efficiency (%)
2	0.37	14.19	1.76	12.39
3	0.75	56.79	7.2	12.67
4	1.03	107.37	15.07	14.03
5	1.41	199.65	25.5	12.7

Fig. 4 **a** Photograph of the flutter of the FM-ATENG moving with the non-post-treated fibrous mat surface. **b** Output voltage of the nontreated FM-ATENGs tested over 1000 s at 3 m/s of airflow. **c** Output voltage of the post-treated FM-ATENGs tested over 1000 s at 3 m/s of airflow. **d** Calculated power with extrinsic load resistance at airflow rates of 2–5 m/s. **e** Voltage of charging capacitors (4.7 μF) measured at airflow rates of 2–5 m/s. **f** Photograph of LEDs powered by FM-ATENGs with 2 m/s of airflow
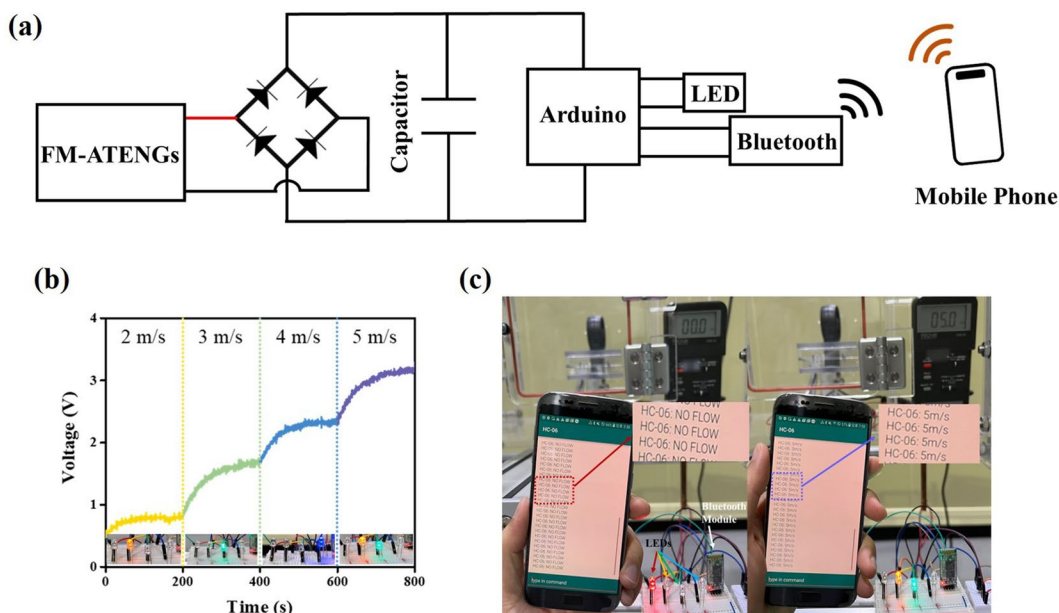
Fig. 5 a Circuit diagram displaying the connection of the FM-ATENGs and electrical parts. **b** Output voltage of FM-ATENGs at different airflow rates, with insets showing photographs of the LEDs activating the airflow checks using FM-ATENGs and an Arduino. **c** Photographs of the airflow check data being sent to a mobile phone through an Arduino using FM-ATENGs

Thus, the flutter does not adhere to the post-treated nylon-11 fibrous mat (Fig. 4b and c).

The output voltage of the FM-ATENG post-treatment nylon-11 fibrous mat was tested for 1000 s to verify its stability. The generated energy was converted into power by varying the load resistance (R_L) from 2 MΩ to 960 MΩ (Fig. 4d). The maximum power was displayed using 10 MΩ of resistance; these were 0.44 µW at 2 m/s, 0.90 µW at 3 m/s, 1.37 µW at 4 m/s, and 1.76 µW at 5 m/s of airflow. Figure 4e depicts the capacitor (4.7 µF) charged by the FM-ATENGs at various airflow rates. Furthermore, LEDs were illuminated to confirm the power generation of the FM-ATENGs. Twenty-four white LEDs were powered by the FM-ATENGs at an airflow velocity of 2 m/s (Fig. 4f, Fig. S2, and Video S2).

As shown in Fig. 5a, the circuit comprised FM-ATENGs, a full-bridge rectifier, a capacitor, a Bluetooth module, LEDs, and an Arduino. As FM-ATENGs generate different amounts of energy depending on the airflow, the amount of charge in the capacitor varies. The FM-ATENGs were connected to an Arduino to act as a switch, and the LEDs were turned on based on the charging level detected by the airflow-check sensors (Fig. 5b and S10). The airflow rate data was received by a mobile phone via the Bluetooth module in the Arduino (Fig. 5c, Fig. S11, and Video S3). The performance of our FM-TENGs is comparable to those presented in previous studies (Table S1), particularly at low starting airflow rates suitable for HVAC systems. Thus, the designed FM-ATENGs may be used as airflow sensors for monitoring the internal airflow in buildings, and a wireless self-powered sensor module may be applied through the stack of FM-ATENGs.

Conclusions

In summary, FM-ATENGs were fabricated for use as airflow check sensors in HVAC ducts. To enhance the electrical output performance, the ferroelectric materials PVDF-TrFE and nylon-11 were selected as opposing materials in the triboelectric series. The conducting polymer PEDOT:PSS was added to PVDF-TrFE to improve its ferroelectric properties, and XRD and FT-IR analyses revealed an enhancement in the ferroelectric β phase of PVDF-TrFE due to the addition. Electrospinning was employed to fabricate a fibrous mat of PVDF-TrFE/PEDOT:PSS and nylon-11 to increase the effective contact surface area. Owing to the poor interfacial adhesion and mechanical strength of the fibrous mat, the surface was modified using an electrospray-based post-treatment, enabling better adhesion between the fibers. The surface of the nylon-11 fibrous mat was modified by electrospraying for 10 s, resulting in improved electrical output performance and sufficient adhesion between the fibers during friction with opposing materials. The optimal FM-TENG demonstrated electrical output performances of 550 V

and 28 μA at 20 Hz. Furthermore, the power density was calculated to be 873 μW/cm^2 at 5 MΩ. The FM-ATENGs comprised fibrous mats that began to flutter steadily at an airflow velocity of 2 m/s. To demonstrate the practical application of the proposed strategy, FM-ATENGs were effectively used in airflow check sensors equipped with a capacitor that charged when the airflow rate was detected. This allows for continuous monitoring of the HVAC status, with the data transmitted to a mobile phone. Devices based on these FM-ATENGs can enable a better control of HVAC systems in buildings, leading to improved energy efficiency without the need for frequent battery replacement and downtime.

Data availability The data sets generated and/or analyzed in this study are available from the corresponding author on reasonable request.

Declarations

Conflict of Interest The authors declare that they have no known competing financial interests or personal relationships that could have appeared to influence the work reported in this paper.

References

1. Li Z, Wang P, Zhang J, Mu S. A strategy of improving indoor air temperature prediction in HVAC system based on multivariate transfer entropy. *Build Environ*. **2022**;*219*: 109164.
2. Jazizadeh F, Joshi V, Battaglia F. Adaptive and distributed operation of HVAC systems: energy and comfort implications of active diffusers as new adaptation capacities. *Build Environ*. **2020**;*186*: 107089.
3. Petrini F, Gkoumas K. Piezoelectric energy harvesting from vortex shedding and galloping induced vibrations inside HVAC ducts. *Energy Build*. **2018**;*158*:371.
4. Ono E, Mihara K, Lam KP, Chong A. The effects of a mismatch between thermal comfort modeling and HVAC controls from an occupancy perspective. *Build Environ*. **2022**;*220*: 109255.
5. Fei F, Zhou S, Mai JD, Li WJ. Development of an indoor airflow energy harvesting system for building environment monitoring. *Energies*. **2014**;*7*:2985.
6. Matiko JW, Grabham NJ, Beeby SP, Tudor MJ. Review of the application of energy harvesting in buildings. *Meas Sci Technol*. **2014**;*25*: 012002.
7. Ahmed A, Hassan I, El-Kady MF, Radhi A, Jeong CK, Selvaganapathy PR, Zu J, Ren S, Wang Q, Kaner RB. Integrated triboelectric nanogenerators in the era of the internet of things. *Adv Sci*. **2019**;*6*:1802230.
8. Cao X, Jie Y, Wang N, Wang ZL. Triboelectric nanogenerators driven self-powered electrochemical processes for energy and environmental science. *Adv Energy Mater*. **2016**;*6*:1600665.
9. Wang W, Yu A, Zhai J, Wang ZL. Recent progress of functional fiber and textile triboelectric nanogenerators: towards electricity power generation and intelligent sensing. *Adv Fiber Mater*. **2021**;*3*:394.
10. Fan FR, Tang W, Wang ZL. Flexible nanogenerators for energy harvesting and self-powered electronics. *Adv Mater*. **2016**;*28*:4283.
11. Sohel Rana SM, Toyabur Rahman M, Salauddin M, Sharma S, Maharjan P, Bhatta T, Cho H, Park C, Yeong PJ. Electrospun PVDF-TrFE/MXene Nanofiber Mat-based triboelectric nanogenerator for smart home appliances. *ACS Appl Mater Interfaces*. **2021**;*13*:4955.
12. Wang S, Mu X, Yang Y, Sun C, Gu AY, Wang ZL, Wang S, Yang Y, Wang ZL, Mu X, Sun C, Gu AY. Flow-driven triboelectric generator for directly powering a wireless sensor node. *Adv Mater*. **2015**;*27*:240.
13. Wang J, Wang H, Yin K, Zi Y. Tribo-induced color tuner toward smart lighting and self-powered wireless sensing. *Adv Sci*. **2021**;*8*:2004970.
14. Wang M, Zhang J, Tang Y, Li J, Zhang B, Liang E, Mao Y, Wang X. Air-flow-driven triboelectric nanogenerators for self-powered real-time respiratory monitoring. *ACS Nano*. **2018**;*12*:6156.
15. Sun L, Huang H, Ding Q, Guo Y, Sun W, Wu Z, Qin M, Guan Q, You Z. Highly transparent, stretchable, and self-healable ionogel for multifunctional sensors, triboelectric nanogenerator, and wearable fibrous electronics. *Adv Fiber Mater*. **2021**;*4*:98.
16. Cho S, Shin Y, Choi J, Eom J, Oh BS, Lee J, Jung GY. Triboelectric nanogenerator based on intercalated Al layer within fluttering dielectric film. *Nano Energy*. **2020**;*77*: 105184.
17. Zhao X, Zhang D, Xu S, Qian W, Han W, Yang Y. Self-powered wireless monitoring of obstacle position and state in gas pipe via flow-driven triboelectric nanogenerators. *Adv Mater Technol*. **2020**;*5*:2000466.
18. An T, Anaya DV, Gong S, Yap LW, Lin F, Wang R, Yuce MR, Cheng W. Self-powered gold nanowire tattoo triboelectric sensors for soft wearable human-machine interface. *Nano Energy*. **2020**;*77*: 105295.
19. Zhou Z, Wang P, Li J, Wang C, Chen J, Zhu L, Zhu H, Zhang D. A self-powered microbiosensor system for specific bacteria detection based on triboelectric nanogenerator. *Nano Energy*. **2022**;*98*: 107317.
20. Li J, Chen J, Guo H. Triboelectric nanogenerators for harvesting wind energy: recent advances and future perspectives. *Energies*. **2021**;*14*:6949.
21. Tcho I-W, Kim W-G, Kim J-K, Kim D-W, Yun S-Y, Son J-H, Choi Y-K. A flutter-driven triboelectric nanogenerator for harvesting energy of gentle breezes with a rear-fixed fluttering film. *Nano Energy*. **2022**;*98*: 107197.
22. Zou H, Zhang Y, Guo L, Wang P, He X, Dai G, Zheng H, Chen C, Wang AC, Xu C, Wang ZL. Quantifying the triboelectric series. *Nat Commun*. **2019**;*10*:1427.
23. Li Y, Zhao Z, Liu L, Zhou L, Liu D, Li S, Chen S, Dai Y, Wang J, Wang ZL. Improved output performance of triboelectric

nanogenerator by fast accumulation process of surface charges. *Adv Energy Mater*. **2021**;*11*:2100050.

24. Kim M, Park D, Alam MM, Lee S, Park P, Nah J. Remarkable output power density enhancement of triboelectric nanogenerators via polarized ferroelectric polymers and bulk MoS 2 composites. *ACS Nano*. **2019**;*13*:4640.

25. Ryu H, Lee JH, Kim TY, Khan U, Lee JH, Kwak SS, Yoon HJ, Kim SW. High-performance triboelectric nanogenerators based on solid polymer electrolytes with asymmetric pairing of ions. *Adv Energy Mater*. **2017**;*7*:1700289.

26. Ibrahim M, Jiang J, Wen Z, Sun X. Surface engineering for enhanced triboelectric nanogenerator. *Nanoenergy Adv*. **2021**;*1*:58.

27. Abir SSH, Sadaf MUK, Saha SK, Touhami A, Lozano K, Uddin MJ. Nanofiber-based substrate for a triboelectric nanogenerator: high-performance flexible energy fiber mats. *ACS Appl Mater Interfaces*. **2021**;*13*:60401.

28. Huang T, Wang C, Yu H, Wang H, Zhang Q, Zhu M. Human walking-driven wearable all-fiber triboelectric nanogenerator containing electrospun polyvinylidene fluoride piezoelectric nanofibers. *Nano Energy*. **2015**;*14*:226.

29. Guo Y, Guo Y, He W, Zhao Y, Shen R, Liu J, Wang J. PET/ TPU nanofiber composite filters with high interfacial adhesion strength based on one-step co-electrospinning. *Powder Technol*. **2021**;*387*:136.

30. Li Z, Shen J, Abdalla I, Yu J, Ding B. Nanofibrous membrane constructed wearable triboelectric nanogenerator for high performance biomechanical energy harvesting. *Nano Energy*. **2017**;*36*:341.

31. Nauman S, Lubineau G, Alharbi HF. Post-processing strategies for the enhancement of mechanical properties of ENMs (electrospun nanofibrous membranes): a review. *Membranes*. **2021**;*11*:39.

32. Li Y, Shen Q, Shen J, Ding X, Liu T, He J, Zhu C, Zhao D, Zhu J. Multifunctional fibroblasts enhanced via thermal and freeze-drying post-treatments of aligned electrospun nanofiber membranes. *Adv Fiber Mater*. **2021**;*3*:26.

33. Li C, Guo H, Wu Z, Wang P, Zhang D, Sun Y. Self-healable triboelectric nanogenerators: marriage between self-healing polymer chemistry and triboelectric devices. *Adv Funct Mater*. **2023**;*33*:2208372.

34. Park D, Kim MC, Kim M, Park P, Nah J. Performance enhancement of flexible polymer triboelectric generator through polarization of the embedded ferroelectric polymer layer. *Appl Sci*. **2021**;*11*:1284.

35. Wang C, Guo H, Wang P, Li J, Sun Y, Zhang D. An advanced strategy to enhance TENG output: reducing triboelectric charge decay. *Adv Mater*. **2023**;*35*:2209895.

36. Chen A, Zhang C, Zhu G, Wang ZL. Polymer materials for high-performance triboelectric nanogenerators. *Adv Sci*. **2020**;*7*:2000186.

37. Jiang Y, Zhou M, Shen Z, Zhang X, Pan H, Lin YH. Ferroelectric polymers and their nanocomposites for dielectric energy storage applications. *APL Mater*. **2021**;*9*: 020905.

38. Choi YS, Kar-Narayan S. Nylon-11 nanowires for triboelectric energy harvesting. *EcoMat*. **2020**;*2*: e12063.

39. Tu NDK, Park J, Na S, Kim KM, Kwon TH, Ko H, Kang SJ. Co-solvent induced piezoelectric γ-phase nylon-11 separator for sodium metal battery. *Nano Energy*. **2020**;*70*: 104501.

40. Chung MH, Kim HJ, Yoo S, Jeong H, Yoo KH. Enhancement of triboelectricity based on fully organic composite films with a conducting polymer. *RSC Adv*. **2022**;*12*:2820.

41. Pepin J, Miri V, Lefebvre JM. New insights into the brill transition in polyamide 11 and polyamide 6. *Macromolecules*. **2016**;*49*:564.

42. Chen S, Yao K, Tay FEH, Chew LLS. Comparative investigation of the structure and properties of ferroelectric poly(vinylidene fluoride) and poly(vinylidene fluoride-trifluoroethylene) thin films crystallized on substrates shutting. *J Appl Polym Sci*. **2010**;*116*:3331.

43. Lanceros-Méndez S, Mano JF, Costa AM, Schmidt VH. FTIR and DSC studies of mechanically deformed β-PVDF films. *J Macromol Sci Part B*. **2001**;*40*:517.

44. Shepelin NA, Sherrell PC, Goudeli E, Skountzos EN, Lussini VC, Dicinoski GW, Shapter JG, Ellis AV. Printed recyclable and self-poled polymer piezoelectric generators through single-walled carbon nanotube templating. *Energy Environ Sci*. **2020**;*13*:868.

45. Shepelin NA, Glushenkov AM, Lussini VC, Fox PJ, Dicinoski GW, Shapter JG, Ellis AV. New developments in composites, copolymer technologies and processing techniques for flexible fluoropolymer piezoelectric generators for efficient energy harvesting. *Energy Environ Sci*. **2019**;*12*:1143.

46. Choi YS, Jing Q, Datta A, Boughey C, Kar-Narayan S. A triboelectric generator based on self-poled Nylon-11 nanowires fabricated by gas-flow assisted template wetting. *Energy Environ Sci*. **2017**;*10*:2180.

47. Lee J-H, Hinchet R, Yun Kim T, Ryu H, Seung W, Yoon H-J, Kim S-W, Lee JH, Kim TY, Kim SW, Hinchet R, Ryu H, Seung W, Yoon HJ. Control of skin potential by triboelectrification with ferroelectric polymers. *Adv Mater*. **2015**;*27*:5553.

48. Kim J, Ryu H, Lee JH, Khan U, Kwak SS, Yoon HJ, Kim SW. High permittivity CaCu3Ti4O12 particle-induced internal polarization amplification for high performance triboelectric nanogenerators. *Adv Energy Mater*. **2020**;*10*:1903524.

49. Chen BD, Tang W, Zhang C, Xu L, Zhu LP, Yang LJ, He C, Chen J, Liu L, Zhou T, Wang ZL. Au nanocomposite enhanced electret film for triboelectric nanogenerator. *Nano Res*. **2018**;*11*:3096.

50. Shao H, Fang J, Wang H, Lin T. Effect of electrospinning parameters and polymer concentrations on mechanical-to-electrical energy conversion of randomly-oriented electrospun poly(vinylidene fluoride) nanofiber mats. *RSC Adv*. **2015**;*5*:14345.

51. Zhang X-S, Han M-D, Wang R-X, Zhu F-Y, Li Z-H, Wang W, Zhang H-X. Frequency-multiplication high-output triboelectric nanogenerator for sustainably powering biomedical microsystems. *Nano Lett*. **2013**;*13*:1168.

52. Xue C, Li J, Zhang Q, Zhang Z, Hai Z, Gao L, Feng R, Tang J, Liu J, Zhang W, Sun D. A novel arch-shape nanogenerator based on piezoelectric and triboelectric mechanism for mechanical energy harvesting. *Nanomaterials*. **2014**;*5*:36.

53. Wang D, Zhang D, Guo J, Hu Y, Yang Y, Sun T, Zhang H, Liu X. Multifunctional poly(vinyl alcohol)/Ag nanofibers-based triboelectric nanogenerator for self-powered MXene/tungsten oxide nanohybrid NO$_2$ gas sensor. *Nano Energy*. **2021**;*89*: 106410.

Moon Hyun Chung received his Ph.D. degree in the Department of Physics from Yonsei University, Seoul, the Republic of Korea, in 2023. Now, he is a postdoctoral researcher at GASOLIQ Co., Ltd. His research interest includes self-powered devices, fiber, immersion cooling, transparent electrode, and nanotechnology.

Seunghwan Yoo received his Ph.D. degree in the Department of Physics from Yonsei University, Seoul, the Republic of Korea, in 2022. Now, he is working as a principal researcher at Korea Institute of Energy Research (KIER). His research interest concentrates on the polymer-based energy harvesting, the design of energy-related composite materials, and self-powered sensor networks.

Hakgeun Jeong received his Ph.D. degree in the Department of Mechanical Engineering from the Seoul National University, Seoul, the Republic of Korea in 2013. Now he is the Director of Energy Efficiency Research Division at the Korea Institute of Energy Research (KIER). His current research interests mainly focus on energy management, energy conversion, and energy network system.

Woo-Nam Jung received his M.S degree in the Department of Mechanical Engineering from Korea University, Seoul, the Republic of Korea, in 2013. Now he is a Ph.D. candidate in Korea Advanced Institute of Science and Technology (KAIST), and a senior researcher at Korea Institute of Energy Research (KIER). His current research interests are combustion-related thermal energy systems.

Kyung-Hwa Yoo received her B.S. degree in the Department of Physics from Yonsei University, Seoul, the Republic of Korea, in 1982 and Ph.D. degree from University of Illinois at Urbana-Champaign, USA, in 1985. She worked as a principal researcher at Korea Research Institute of Standards and Science from 1987 to 2001. In 2001, she moved to Yonsei University. Now, she is a professor in physics department at Yonsei University. Her current research interests include nanoelectronic devices and nanobio-/nanomedical technology.